From a eutectic mixture to a deep eutectic system via anion selection

The Journal of Chemical Physics

From a eutectic mixture to a deep eutectic system via anion selection: Glutaric acid + tetraethylammonium halides

Cite as: J. Chem. Phys. **155**, 014502 (2021); https://doi.org/10.1063/5.0050533
Submitted: 16 March 2021 . Accepted: 09 June 2021 . Published Online: 01 July 2021

Adriaan van den Bruinhorst, Laura J. B. M. Kollau, Mark Vis, Marco M. R. M. Hendrix, Jan Meuldijk, Remco Tuinier, and A. Catarina C. Esteves

The Journal of Chemical Physics ARTICLE scitation.org/journal/jcp

From a eutectic mixture to a deep eutectic system via anion selection: Glutaric acid + tetraethylammonium halides

Cite as: J. Chem. Phys. 155, 014502 (2021); doi: 10.1063/5.0050533
Submitted: 16 March 2021 • Accepted: 9 June 2021 •
Published Online: 1 July 2021

Adriaan van den Bruinhorst,[1,2,a] Laura J. B. M. Kollau,[1,3] Mark Vis,[1,4] Marco M. R. M. Hendrix,[4,5] Jan Meuldijk,[6] Remco Tuinier,[1,4,b] and A. Catarina C. Esteves[1,4]

AFFILIATIONS

[1] Laboratory of Physical Chemistry, Department of Chemical Engineering and Chemistry, Eindhoven University of Technology, P.O. Box 513, 5600 MB Eindhoven, The Netherlands
[2] Theoretical Chemistry, Chemistry Laboratory, École Normale Supérieure de Lyon & CNRS, 69007 Lyon, France
[3] Cirular Engineering Group, Faculty of Science and Engineering, Maastricht University, Maastricht, The Netherlands
[4] Institute for Complex Molecular Systems, Eindhoven University of Technology, P.O. Box 513, 5600 MB Eindhoven, The Netherlands
[5] Self-Organising Soft Matter, Department of Chemical Engineering and Chemistry, Eindhoven University of Technology, P.O. Box 513, 5600 MB Eindhoven, The Netherlands
[6] Polymer Reaction Engineering, Department of Chemical Engineering and Chemistry, Eindhoven University of Technology, P.O. Box 513, 5600 MB Eindhoven, The Netherlands

Note: This paper is part of the JCP Special Topic on Chemical Physics of Deep Eutectic Solvents.
[a] **Electronic mail:** a.v.d@bruinhorst.com
[b] **Author to whom correspondence should be addressed:** r.tuinier@tue.nl

ABSTRACT

In pursuit of understanding structure–property relationships for the melting point depression of binary eutectic mixtures, the influence of the anion on the solid–liquid (S–L) phase behavior was explored for mixtures of glutaric acid + tetraethylammonium chloride, bromide, and iodide. A detailed experimental evaluation of the S–L phase behavior revealed that the eutectic point is shifted toward lower temperatures and higher salt contents upon decreasing the ionic radius. The salt fusion properties were experimentally inaccessible owing to thermal decomposition. The data were inter- and extrapolated using various models for the Gibbs energy of mixing fitted to the glutaric-acid rich side only, which allowed for the assessment of the eutectic point. Fitting the experimental data to a two-parameter Redlich–Kister expansion with Flory entropy, the eutectic depth could be related to the ionic radius of the anion. The anion type, and in particular its size, can therefore be viewed as an important design parameter for the liquid window of other acid and salt-based deep eutectic solvents/systems.

I. INTRODUCTION

The term deep eutectic solvents (DESs) was coined at the beginning of this century.[1] This has caused a paradigm shift in the application of eutectic mixtures; their liquid phase has since then been regarded as the solvent phase. The exact definition of DESs is still under discussion;[2–4] here, we adopt the following: *Deep* eutectic solvents/systems are mixtures that melt significantly below the ideal eutectic temperature. Being eutectic mixtures, the melting point of DESs is lower than that of its pure constituents, showing a minimum at the eutectic composition. As many binary mixtures show eutectic behavior, this has given rise to a wide variety of applications in addition to the traditional use of eutectic systems. Up to some extent, DES properties (e.g., viscosity, electric conductivity, and density) can be tailored to an application by adapting the composition or by choosing the appropriate components. The

current development of novel DESs is mostly application driven, while a rational design of DESs is viable only once structure–property relationships are established.

The solid–liquid (S–L) phase behavior of a eutectic mixture determines the compositions and temperatures at which it can be applied as a liquid. The phase diagram of a DES, and with it its *eutectic depth*, can be steered by the proper selection of its constituents. Although the evaluation of the S–L phase diagram for novel eutectic solvents is gradually becoming the norm, systematic studies on how the S–L phase behavior of DESs depends on its constituents are relatively scarce. A study on mixtures of dicarboxylic acids and quaternary ammonium bromide salts showed that the liquid window is mostly controlled by the acidity of the carboxylic proton, the displacement of the bromide, and the bulkiness of the cation.[5] Other work showed that changing the alkyl-chain length of fatty acids and tetra-alkyl bromide ammonium salts has a moderate effect on the eutectic phase behavior when mixed with a weak hydrogen bond donor.[4,6] This is corroborated by the minimal interactions between the alkyl side-chains of the ammonium cation and the acceptor site of urea[7] and minor interactions between carboxylate anions and ammonium cations in solution.[8] However, when two quaternary ammonium salts are combined, the cation functionalization has a large effect on the resulting phase diagram via the chloride anion.[9] Other studies have as well ascribed a pivotal role to the chloride anion in eutectic systems, in both the resulting liquid structure and bulk properties.[7,10,11] Abbott *et al.*[1] hinted on a strong influence of the anion on the S–L phase behavior of choline salts + urea derivates. However, only mixtures with a molar ratio of 2:1 have been evaluated, while the eutectic point is not limited by stoichiometry and a wide composition range should be considered to gain insight into the S–L phase behavior.

Inspired by the choline-based systems, we studied mixtures of glutaric acid (GluA) and tetraethylammonium halide salts (Et_4NX) in the present work (Fig. 1). GluA is a naturally occurring dicarboxylic acid that was selected because it exhibits versatile phase behavior when mixed with other organic components, ranging from eutectic mixtures[12–17] to liquid miscibility gaps[12,13] and co-crystals.[18–23] Eutectic mixtures of GluA and choline chloride (ChCl) show strong melting point depressions.[14,16] However, carboxylic acids can react with the alcohol moiety of choline,[16,24] which is why the more inert tetra-alkylammonium salt was selected instead of ChCl. Previous work[25] showed that GluA + Et_4NCl forms a chemically and physically stable liquid at room temperature, implying a large melting point depression and strong negative deviations from ideal eutectic behavior.

It may be expected that exchanging the Cl^- anion with the bulkier Br^- and I^- significantly affects the eutectic phase behavior. To elucidate this shift, the S–L phase diagrams of GluA + Et_4NCl, GluA + Et_4NBr, and GluA + Et_4NI were constructed experimentally over a broad composition range using a wide variety of analysis techniques. Additionally, the solid phase was evaluated using wide-angle x-ray scattering (WAXS) at miscellaneous temperatures and compositions since both GluA and Et_4NX are polymorphic materials[26–29] and can form co-crystals.[18–23,30] The resulting phase boundaries were described quantitatively using various suitable thermodynamic models.[31,32] Through these steps, the influence of the anion on the transition from an ideal to a *deep* eutectic mixture was unraveled.

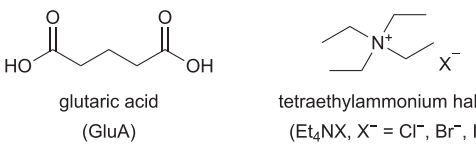

FIG. 1. Structural formula and abbreviations of the studied components.

II. EXPERIMENTAL

A. Chemicals

GluA (>99%), Et_4NI (>98%), Et_4NBr (>98%), and Et_4NCl (>98%) were purchased from Sigma-Aldrich and dried for more than 48 h under high vacuum at 293–298 K before usage. Using a Metrohm 899 coulometric Karl-Fischer titrator with a Merck CombiCoulomat fritless medium, the water mass fractions of the dried solids were determined from ethanol solutions ($w_{solid} \approx 20\%$) to be ~800, 185, and 70 ppm for GluA, Et_4NBr, and Et_4NCl, respectively. Anhydrous ethanol (>99.5%, $w_{H_2O} \approx 90$ ppm) was also acquired from Sigma-Aldrich, and all chemicals were stored in a glovebox under a dry nitrogen atmosphere ($w_{H_2O} < 2$ ppm, typically <0.1 ppm). Cyclohexane (100%, gas-chromatography) was obtained from TCI chemicals.

B. Sample preparation

All samples were prepared in a glovebox under a dry nitrogen atmosphere. The pure components were weighed separately on an analytical balance with a resolution of 0.1 mg before being mixed at the desired composition. GluA + Et_4NI and GluA + Et_4NBr samples were typically mixed by grinding the weighed solids with a mortar and pestle at ambient temperature (291–295 K). The solid mixtures were either used directly or stored in glass vials and added to the appropriate sample holders when needed for analysis. Depending on the ratio of its constituents, GluA + Et_4NCl would (partially) liquefy upon mixing at ambient temperatures. This resulted in a sticky paste, a viscous liquid with solids, or a clear liquid. Samples that could be liquefied at temperatures at or below 333 K were handled as a liquid.

C. Thermal analysis

1. Thermal stability

The thermal stability of the samples was evaluated with thermogravimetric analysis (TGA) using a TA instruments Q500 TGA, the furnace was continuously flushed with 40 ml min^{-1} dry nitrogen. The temperature and weight accuracies were 0.1 K and 2 μg. The sample holder was tared, and then the sample (10–20 mg) was prepared and transported to the equipment in a concealed vial under a dry nitrogen atmosphere. While loading the sample into the furnace, it could not be prevented that the sample was shortly (<2 min) exposed to the lab atmosphere. The TGA data were acquired at a heating rate ($d\Phi/dt$) of $d\Phi/dt = 1$ K min^{-1}.

2. Differential scanning calorimetry

A TA Instruments Q2000 differential scanning calorimeter (DSC) was used, equipped with a liquid nitrogen cooling system

(LNCS). The cell was continuously flushed with 50 ml min^{-1} dry nitrogen. Samples of 5–7 mg were crimped into a hermetic Tzero pan under a dry nitrogen atmosphere, and an empty pan was used as the reference. The samples were subsequently subjected to a sample-specific heating program. Typically, $dT/dt = 1$ K min^{-1} was applied, but other heating rates were explored as well. The melting points and solid–solid (S–S) transitions of the pure components as well as the solidus temperatures of the eutectic mixtures were determined from the onset temperature of the corresponding peak in the DSC thermogram unless stated otherwise. The liquidus temperatures were extracted from the inflection point, i.e., the minimum of the temperature derivative of the heat flow at the descent of the liquidus peak. A detailed description of the instrument calibration, temperature programs, and data processing can be found in the supplementary material. After data acquisition, the DSC pan was cut open and its contents were dissolved in 1 ml of D_2O for composition analysis with ^{1}H-NMR.

3. Centrifuge method

Previous work[33] gives a detailed description of this method. The centrifuge tubes were sealed in a dry and inert atmosphere, and the applied temperature calibration is described in Sec. 1.2 of the supplementary material.

4. Cloud-point method

Mixtures of 5 g with known composition were kept at constant temperature under magnetic stirring at 250 rpm by an IKA RCT basic hot plate with an ETS D-5 controller immersed in a stirred vial with glycerol (accuracy ±0.5 K, precision 0.1 K). 0.01–0.1 g of pure solid was added to the liquid, after which the mixture was equilibrated. The mixture was then visually inspected; smaller additions and longer equilibration times were applied if the solids did not readily dissolve. When the necessary equilibration time exceeded 3 h, the sample was left overnight. If the sample remained turbid, we considered that the liquidus phase boundary was crossed. The composition was followed by correcting the initial composition with the sum of the additions. The final liquidus composition was determined by ^{1}H-NMR spectroscopy for a small liquid sample (collected without solids).

D. Crystal structure analysis

Crystal structures of the pure components and binary mixtures were analyzed with WAXS. WAXS data were collected using a SAXSLAB GANESHA vacuum system with a Pilatus 300 K solid-state photon-counting 2D detector using a high brilliance Microfocus Cu Source, Xenocs Genix3D, wavelength 1.541 84 Å. Measurements were performed in the transmission mode using a sample to detector distance of ~60 mm and an exposure time of 15 min. Prior to each measurement series, a silver behenate standard was used to correct for deviations in the sample to detector distance. The scattering intensity was measured as a function of the momentum transfer vector: $q = 4\pi \sin\theta/\lambda$, where λ is the radiation wavelength and θ is the scattering angle. Samples were transferred into a 1 mm, thin-walled (0.01 mm thickness), glass capillary. The capillaries were prepared under a dry nitrogen atmosphere in a glovebox and sealed using a dot of thermal glue before being transferred to atmospheric conditions. The capillaries were loaded horizontally into a Linkam temperature controlled stage connected to a Dewar vessel with liquid nitrogen as the coolant. A temperature program was set for each sample using a heating rate of 1 K min^{-1} and a cooling rate of 10 K min^{-1}, and the samples were equilibrated for 10 min at each temperature.

E. Composition analysis

1. 1H-NMR spectroscopy

Samples were dissolved in ~1 ml D_2O and added to a 5 mm thin-walled economic Wilmad NMR tube. A Bruker BZH 400/52 spectrometer equipped with an autosampler carousel was used, and the spectra were recorded in 16 scans with a relaxation time of 5 s. The TopSpin software used to control the equipment auto-shimmed and auto-phased the spectra. The peaks were integrated using the MestReNova 10.0.2 software after applying a Withaker Smoother baseline correction and small phase corrections if necessary. Peak assignments and the translation of peak integrals to mole fractions are described in the supplementary material.

2. Water content

Water content was determined via Karl-Fischer titration using a Metrohm 899 coulometer equipped with a generator electrode without a diaphragm. Merck CombiCoulomat fritless was used as the titration medium. 1 g of solids was dissolved in 4 g anhydrous ethanol prior to measurement. Approximately 1 g solution was injected per measurement. For each sample, the average value of at least three measurements was taken into account. The water content of the solids was calculated from mass balance accounting for the water content of ethanol (typically 90 ppm).

III. THERMODYNAMIC MODELING

At the S–L binodal (liquidus phase boundary), the solid and liquid phases are in equilibrium and the corresponding chemical potentials of each component, μ_i, are equal,

$$\mu_i^{\mathrm{S}} = \mu_i^{\mathrm{L}}. \tag{1}$$

In simple eutectic systems, the solid phase is completely immiscible. Therefore, the chemical potential of solid i equals that of the pure solid, $\mu_i^{\mathrm{S}} = \mu_i^{*,\mathrm{S}}$. Since the liquid phase is considered to be completely miscible, the chemical potential of component i in the liquid follows from the molar Gibbs energy of mixing,[34] g^L, as

$$\mu_i^{\mathrm{L}} = \mu_i^{*,\mathrm{L}} + \frac{\partial(ng^{\mathrm{L}})}{\partial n_i}\Big|_{T,P,n_{j\neq i}}. \tag{2}$$

By combining Eqs. (1) and (2), the molar Gibbs energy of fusion ($\Delta_{\mathrm{fus}}g_i^*$) and mixing ($g^L$) of the liquid can be related as

$$\frac{\partial(ng^{\mathrm{L}})}{\partial n_i} = \mu_i^{*,\mathrm{S}} - \mu_i^{*,\mathrm{L}}, \tag{3a}$$

$$\left(g^{\mathrm{L}} + (1-x_i)\frac{\partial g^{\mathrm{L}}}{\partial x_i}\right) = -\Delta_{\mathrm{fus}}g_i^*. \tag{3b}$$

We denote $\Delta\mu_i^{\mathrm{L}}$ as the change in the liquid chemical potential of i upon mixing,

$$\Delta\mu_i^{\mathrm{L}} = \mu_i^{\mathrm{L}} - \mu_i^{*,\mathrm{L}} \tag{4a}$$

$$= \left(g^{\mathrm{L}} + (1 - x_i)\frac{\partial g^{\mathrm{L}}}{\partial x_i}\right), \tag{4b}$$

and combining Eqs. (3) and (4) and normalizing with RT yields the liquidus temperature used to describe the eutectic phase diagrams,

$$\frac{\Delta\mu_i^{\mathrm{L}}}{RT} = -\frac{\Delta_{\mathrm{fus}}g_i^*}{RT}, \tag{5a}$$

$$T = -\frac{\Delta_{\mathrm{fus}}g_i^*/R}{\frac{\Delta\mu_i^{\mathrm{L}}}{RT}}. \tag{5b}$$

Here, $\Delta_{\mathrm{fus}}g_i^*$ can be written in terms of the molar enthalpy Δh_i^* and entropy Δs_i^* of fusion. At the melting point T_i^*, $\Delta_{\mathrm{fus}}g_i^*(T_i^*) = \Delta h_i^*(T_i^*) - T_i^*\Delta s_i^*(T_i^*) = 0$. $\Delta_{\mathrm{fus}}g_i^*$ at T can be obtained via the heat capacity difference between the solid and liquid phases $\Delta c_{p,i}^*(T)$,

$$\Delta_{\mathrm{fus}}g_i^*(T) = \Delta h_i^*(T) - T\Delta s_i^*(T)$$
$$= \Delta h_i^*\left(1 - \frac{T}{T_i^*}\right) + \int_{T_i^*}^{T}\Delta c_{p,i}^*(T)dT - T\int_{T_i^*}^{T}\frac{\Delta c_{p,i}^*(T)}{T}dT. \tag{6}$$

Only for GluA, $\Delta c_{p,i}^*(T)$ was taken into account since the c_p of the liquid was inaccessible for the salts. $\Delta c_{p,i}^*(T)$ was described by a first order polynomial,

$$\Delta c_{p,i}^*(T) = A_i^{\mathrm{L}} - A_i^{\mathrm{S}} + \left(B_i^{\mathrm{L}} - B_i^{\mathrm{S}}\right)T$$
$$= 209 - 0.340T, \tag{7}$$

for which the values of parameters A_i^{L}, A_i^{S}, B_i^{L}, and B_i^{S} were adopted from the literature.[26] For the salts, Eq. (6) was approximated as

$$\Delta_{\mathrm{fus}}g_i^* = \Delta h_i^*\left(1 - \frac{T}{T_i^*}\right). \tag{8}$$

When the liquidus temperature falls below the S–S transition temperature of the equilibrium solid, Eqs. (6) and (8) were expanded,

$$\Delta_{\mathrm{fus}}g_i^* = \Delta h_i^*\left(1 - \frac{T}{T_i^*}\right) + \Delta_{\mathrm{tr}}h_i^*\left(1 - \frac{T}{T_{\mathrm{tr},i}^*}\right)$$
$$+ \int_{T_i^*}^{T_{\mathrm{tr},i}^*}\Delta_\alpha^{\mathrm{L}}c_{p,i}^*(T)dT + \int_{T_{\mathrm{tr},i}^*}^{T}\Delta_\beta^{\mathrm{L}}c_{p,i}^*(T)dT$$
$$- T\int_{T_i^*}^{T_{\mathrm{tr},i}^*}\frac{\Delta_\alpha^{\mathrm{L}}c_{p,i}^*(T)}{T}dT - T\int_{T_{\mathrm{tr},i}^*}^{T}\frac{\Delta_\beta^{\mathrm{L}}c_{p,i}^*(T)}{T}dT \tag{9}$$

and

$$\Delta_{\mathrm{fus}}g_i^* = \Delta h_i^*\left(1 - \frac{T}{T_i^*}\right) + \Delta_{\mathrm{tr}}h_i^*\left(1 - \frac{T}{T_{\mathrm{tr},i}^*}\right), \tag{10}$$

where β and α refer to the solid states in the $\beta \to \alpha$ S–S transition (tr).

The g^{L} of the binary mixtures was based on Flory entropy in combination with two expressions for the enthalpic contributions to the molar Gibbs energy of mixing: the zero and first order Redlich–Kister (RK) polynomial[35] and the non-random two-liquid (NRTL) model.[36] The two fitting parameters of RK, k_0 and k_1, respectively, correspond to the binary interaction parameter from regular solution theory, χ, and what can be seen as a three-body interaction parameter that describes enthalpic asymmetries in the molar Gibbs energy of mixing,[32]

$$\frac{g^{\mathrm{L}}}{RT} = x_1\ln\phi_1 + x_2\ln\phi_2 + x_1x_2[k_0 + k_1(x_1 - x_2)], \tag{11}$$

where the volume fraction ϕ_i is defined as

$$\phi_i = \frac{x_i v_i}{\sum_i x_i v_i}, \tag{12}$$

with v_i being the molar volume of component i, assuming isometric mixing. For $k_1 = 0$, Eq. (11) is also called the Margules equation.[37] For NRTL, the molar Gibbs energy of mixing is defined as

$$\frac{g^{\mathrm{L}}}{RT} = x_1\ln\phi_1 + x_2\ln\phi_2 + x_1x_2\left(\frac{\tau_{21}G_{21}}{x_1 + x_2G_{21}} + \frac{\tau_{12}G_{12}}{x_1G_{12} + x_2}\right), \tag{13}$$

where

$$G_{12} = \exp(-\alpha\tau_{12}),$$
$$G_{21} = \exp(-\alpha\tau_{21}), \tag{14}$$

with α being the non-randomness parameter and

$$\tau_{12} = \frac{\Delta g_{12}}{RT},$$
$$\tau_{21} = \frac{\Delta g_{21}}{RT}. \tag{15}$$

Δg_{12} and Δg_{21} are the differences in the interaction energy between mixed pairs (1–2 and 2–1) and the pure pairs (2–2 and 1–1),[36] respectively. However, the values for Δg_{12} and Δg_{21} should be interpreted with care because the NRTL model is prone to solutions with local minima. The phase diagrams fitted with Eq. (13) were therefore optimized using a two-step approach. The first step comprised the identification of the (local) minima for 200 randomly generated initial parameter sets by minimizing the objective function

$$f_{\mathrm{obj,ini}} = \sum_n\left(T\left(T_n^{\mathrm{exp}}, x_{i,n}^{\mathrm{exp}}, p\right) - T_n^{\mathrm{exp}}\right)^2, \tag{16}$$

where n is the number of experimental data points $(T^{\mathrm{exp}}, x^{\mathrm{exp}})$ and p is a vector of fitting parameters. The solution with the lowest residuals was used as initial guess for the final objective function

$$f_{\mathrm{obj}} = \sum_n\left(T\left(T, x_{i,n}^{\mathrm{exp}}, p\right) - T_n^{\mathrm{exp}}\right)^2. \tag{17}$$

The RK model is less sensitive to local minima and could be fitted directly using Eq. (17).

In the diluted regime, deviations from ideal mixing behavior as a result of intermolecular interactions are negligible. However, salts can dissociate and carboxylic acids can associate, e.g., via dimerization. In those cases, colligative properties—such as the melting point depression—are governed by the effective mole fraction of diluted

constituent j. The mole fraction x_j and the effective mole fraction $x_{\mathrm{eff},j}$ can be related via the Van 't Hoff factor, F_{VtH},

$$x_{\mathrm{eff},j} = F_{\mathrm{VtH}} x_j, \tag{18a}$$

$$x_{\mathrm{eff},i} = 1 - F_{\mathrm{VtH}} x_j. \tag{18b}$$

In order to determine whether salt dissociation or acid dimerization should be taken into account, the deviations from ideal eutectic behavior ($F_{\mathrm{VtH}} = 1$) in the dilute regimes were evaluated.

The fusion properties of the Et_4NX salts could not be determined experimentally because they decompose before melting. The fitting parameters were therefore determined by fitting the S–L phase boundary at the GluA-rich side only.

IV. RESULTS AND DISCUSSION

A. Pure components

Prior to studying the eutectic mixtures of GluA and Et_4NX salts, the thermal properties of the pure components were determined and verified with the literature.

1. Glutaric acid

The DSC thermograms of GluA (Fig. S6) exhibit two endothermic phase transitions upon heating: the S–S transition from the β-phase to the α-phase and the melting of the α-phase. The $\beta \rightarrow \alpha$ transition was confirmed with WAXS (Fig. S7), and the diffraction patterns are similar to those in the literature.[27,38] The $\beta \rightarrow \alpha$ transition temperature (343.8 ± 0.8 K) and enthalpy (2.46 ± 0.10 kJ mol^{-1}) are in agreement with literature values, considering that the transition temperature is sensitive to the applied heating rate. The GluA melting point (369.0 K) was slightly lower than that reported in the literature (370.9–372.2 K), while the enthalpy of fusion (21.2 ± 1.0 kJ mol^{-1}) matched literature values (19.8–23 kJ mol^{-1}).[12,26,38,39] GluA was extensively dried but not recrystallized before use, which might be necessary for a higher onset temperature. A table with the relevant literature values and a comprehensive discussion are available in the supplementary material.

2. Tetraethylammonium halides

All studied Et_4NX salts decompose before melting. Et_4NI, Et_4NBr, and Et_4NCl start decomposing at 493, 468, and 450 K, respectively. The weight loss curves (Fig. S9) are similar to those in the literature,[40] but the extracted temperatures are (slightly) lower owing to the difference in the reported heating rate and data extraction methodology. One or two relatively small step-wise weight losses were observed before complete decomposition, and these are unlikely to impact the phase behavior of the studied salts and are discussed in more detail in the supplementary material. The DSC thermograms were obtained until 493, 468, and 443 K for Et_4NI, Et_4NBr, and Et_4NCl, respectively.

For each of the Et_4NX salts, one or more S–S transitions were observed with DSC and WAXS, analogous to other studies[28,29,41,42] where S–S rearrangements have been observed with infrared[28] and solid-state ^{1}H-NMR[41,42] spectroscopy. The recorded DSC thermograms and WAXS patterns can be found in Secs. 2.3–2.5 of the supplementary material, along with tables in which the obtained transition temperatures and enthalpies are compared to those in the literature. Et_4NI showed a clear endothermic S–S transition from phase II to phase I at 466.5 K (23.0 kJ mol^{-1}), and the structural changes in the crystal were confirmed with WAXS. For Et_4NBr, two S–S transitions were observed, one (III → II) at 440 K (19.1 kJ mol^{-1}) and the other (II → I) at 463.3 K (1.5 kJ mol^{-1}), which is at the brink of decomposition. Only the III → II transition was confirmed with WAXS since the stability of the sample could not be guaranteed above 463.3 K under vacuum. Et_4NCl exhibited four endothermic S–S transitions at the first heating cycle, of which only the transition at 394.0 K (7.2 kJ mol^{-1}) reoccurred on the second and third cooling–heating cycles of the DSC thermograms and WAXS patterns. A detailed discussion on the initial S–S transitions can be found in the supplementary material.

For Et_4NI and Et_4NBr, the S–S transitions occur close to the boiling temperature of GluA; hence, it is unlikely that these will affect the S–L phase behavior of their mixtures with GluA at atmospheric conditions. The S–S transition temperature of Et_4NCl lies ~20 K above the melting point of GluA and is present in the S–L phase diagram of GluA + Et_4NCl. In recent studies, the Et_4NCl decomposition temperature[6,43] (527 K) was interpreted as the melting point. In the present work, no liquid formation was observed visually for any of the studied Et_4NX salts and amorphous peaks in the WAXS patterns implying liquid formation were absent. Hence, our results confirm that Et_4NX decomposition occurs before melting[42] (see Fig. S10) and no experimental melting points or enthalpies of fusion can be obtained for these components.

B. Construction of the S–L phase diagrams

1. Glutaric acid + tetraethylammonium iodide

Figure 2 shows the S–L phase diagram of GluA + Et_4NI. Three major transitions can be recognized: the $\beta \rightarrow \alpha$ transition (onset

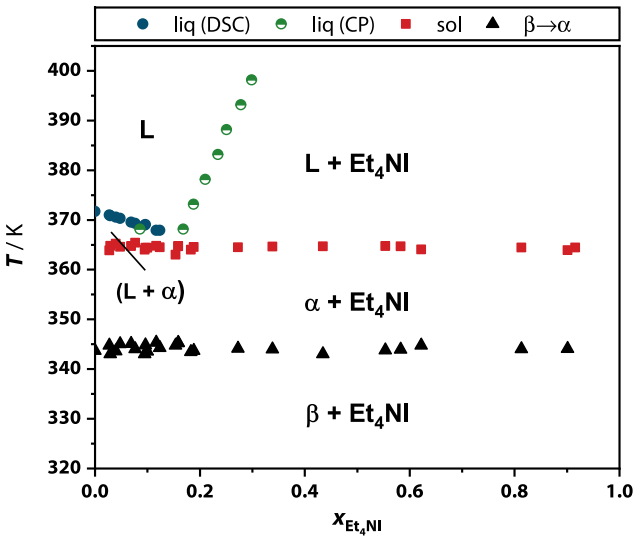

FIG. 2. T–x phase diagram of the glutaric acid + tetraethylammonium iodide (GluA + Et_4NI) system. Three transitions can be recognized: the solid–solid of GluA ($\beta \rightarrow \alpha$, triangles), the solidus (sol, squares), and the liquidus (liq, circles) transition. The phase diagram was constructed with DSC (solid symbols) and the cloud-point method (CP, half-open symbols). Each phase is marked with L (liquid mixture), or α or β (solid GluA), or Et_4NI (solid II-phase).

343 K) of GluA, the solidus transition (onset 365 K), and the liquidus transition. In the DSC thermograms (Fig. 3), the GluA $\beta \rightarrow \alpha$ transition appears at temperatures corresponding to that of pure GluA over the whole composition range. The WAXS patterns (Figs. 4 and S17) clearly show the GluA $\beta \rightarrow \alpha$ transition together with peaks of Et_4NI, emphasizing that the solidus transition occurs above the $\beta \rightarrow \alpha$ transition.

The solidus transition appears slightly below the α–L transition of pure GluA. The corresponding DSC peaks can be recognized in the thermograms over the whole composition range. Upon heating GluA + Et_4NI above the measured solidus temperature, partial liquid formation was observed visually (Fig. S18) as well as via the appearance of broad amorphous peaks in the WAXS patterns on both sides of the eutectic composition.

The construction of the liquidus phase boundary was less straightforward. Up to $x_{Et_4NI} \approx 0.15$, the DSC thermograms exhibited the characteristic solidus and liquidus peaks. However, no liquidus peaks could be observed with DSC in the hypertectic region. This is most likely caused by the low dissolution rate of the Et_4NI in the eutectic liquid. If the dissolution rate is very low, the heat flow rate corresponding to the continuous dissolution of the salt cannot be distinguished from the baseline and only a solidus transition can be recognized with DSC.

The cloud-point method could overcome this limitation: The liquidus phase transition was observed upon an isothermal shift in composition via the addition of excess solid to the eutectic melt. The low dissolution rates were confirmed by the equilibration times

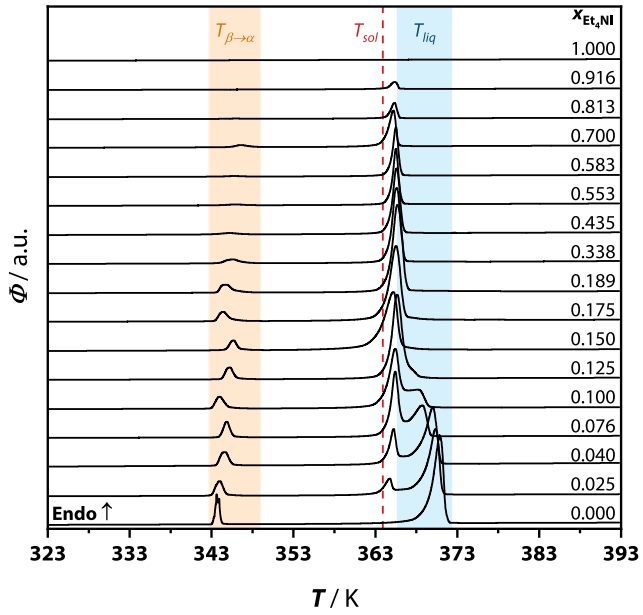

FIG. 3. DSC thermograms—heat flow Φ vs temperature T—of the glutaric acid + tetraethylammonium iodide (GluA + Et_4NI) system at various mole fractions x_{Et_4NI} (endotherms up). The type of transition temperature is identified at the top of the figure: $\beta \rightarrow \alpha$ of GluA, the solidus (sol), and the liquidus (liq) transition. The heating rate was 1 K min^{-1}; note that the composition increment in the top half of the figure is larger than the bottom half.

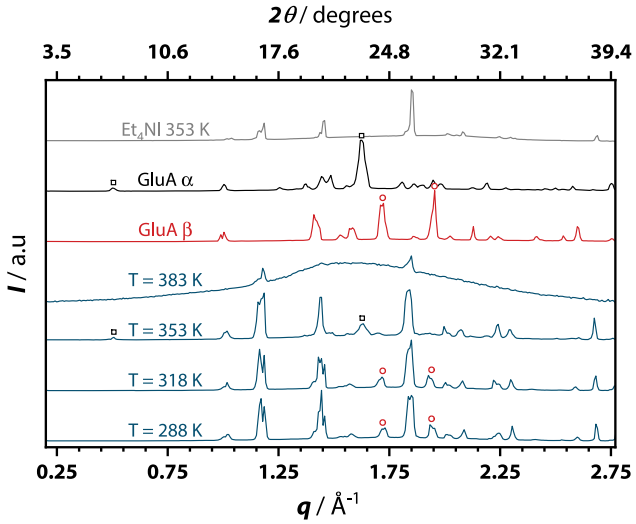

FIG. 4. Wide-angle x-ray scattering patterns of tetraethylammonium iodide (Et_4NI, gray), pure glutaric acid (GluA) in the α (black) and β (red) phases, and their mixture at $x_{Et_4NI} = 0.5$ (blue) at different temperatures. Specific peaks of the pure components are marked for clarity.

at compositions near the liquidus phase transition, which exceeded 1 h for additions of ~0.01 g Et_4NI to a total of 5 g. Additionally, Fig. S18 shows that a mixture of $x_{Et_4NI} = 0.175$ contains solids above the liquidus temperatures when heated at a rate of 0.1 K min^{-1}. Considering the long equilibration times using the cloud-point method, 398 K was the highest temperature at which the liquidus temperature was evaluated. At higher temperatures, evaporation of GluA or decomposition of the salt was anticipated.

The obtained liquidus temperatures suggest that the eutectic point can be found at a composition of $x_{Et_4NI} \approx 0.15$ and a temperature of $T_{eut} \approx 364.5$ K. The eutectic composition could not be extracted from a Tammann plot because the solidus and liquidus peak overlapped too much to determine the enthalpy of each transition separately. Given the constant $\beta \rightarrow \alpha$ and solidus transition temperatures as well as the absence of new peaks in the WAXS patterns, simple eutectic behavior is assumed for GluA + Et_4NI, i.e., no solid solution or co-crystal formation.

2. Glutaric acid + tetraethylammonium bromide

Figure 5 shows the S–L phase diagram of the GluA + Et_4NBr system. Et_4NBr significantly depressed the GluA melting point as compared to Et_4NI. Upon cooling below the solidus temperature, the mixtures did not crystallize readily, hampering DSC analysis within practical timescales. Instead, the samples became supercooled and subsequently vitrified at $T_g \approx 215$ K, also at low heating rates. Crystallization typically only occurred above T_g upon heating (cold-crystallization). An optimized DSC heating/cooling program (supplementary material, Sec. 1.1) allowed the determination of the solidus, $\beta \rightarrow \alpha$, as well as the liquidus temperature.

The solidus transition shows a slight discontinuity near $x_{Et_4NBr} = 0.25$, which was attributed to the supercooling of the GluA α-phase[27] based on WAXS (Fig. S20). The metastable α-phase forms

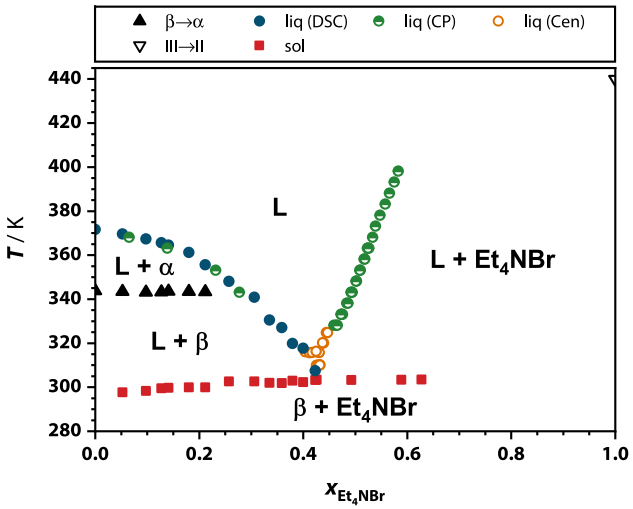

FIG. 5. *T*–*x* phase diagram of the glutaric acid + tetraethylammonium bromide (GluA + Et_4NBr) system. Three types of transitions can be recognized: the solidus (sol, squares), the solid–solid (triangles) of GluA ($\beta \rightarrow \alpha$) and Et_4NBr (III → II), and the liquidus (liq, circles) transition. The phase diagram was constructed with DSC (solid symbols), the cloud-point method (CP, half-open symbols), and the centrifuge method (Cen, open symbols). Each phase is marked with L (liquid mixture), or α or β (solid GluA), or Et_4NBr (solid III-phase).

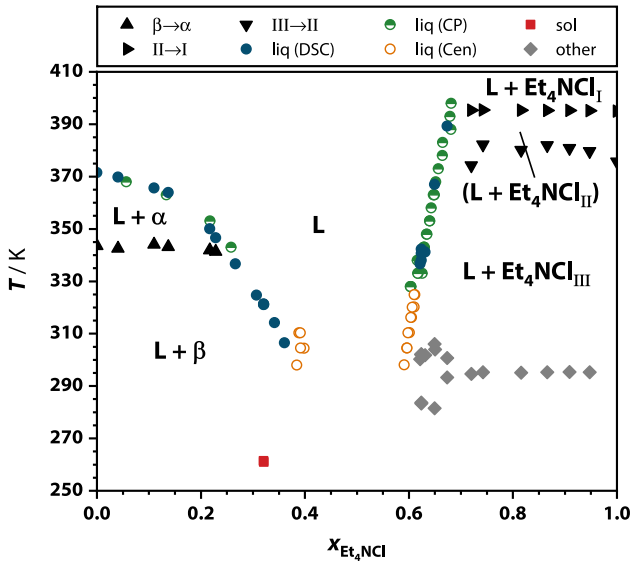

FIG. 6. *T*–*x* phase diagram of the glutaric acid + tetraethylammonium chloride (GluA + Et_4NCl) system. Various transitions were observed: the solidus (sol, squares), the solid–solid (triangles) of GluA ($\beta \rightarrow \alpha$) and Et_4NCl (III → II), the liquidus (liq, circles), and other transitions. The phase diagram was constructed with DSC (solid symbols), the cloud-point method (CP, half-open symbols), and the centrifuge method (Cen, open symbols). Each phase is marked with L (liquid mixture), or α or β (solid GluA), or Et_4NCl_i (solid *i*-phase).

a eutectic with Et_4NBr at a lower temperature than the β-phase. Above the solidus temperature, an exothermic crystal rearrangement toward the thermodynamically stable β-phase was observed with DSC (Fig. S19) as well as with WAXS (Fig. S20). Probably, the liquefaction of Et_4NBr facilitated this rearrangement. The $\beta \rightarrow \alpha$ transition remains at constant temperature until it merges with the liquidus phase boundary, after which the solidus transition also appeared at constant temperature.

The liquidus phase boundary was constructed using DSC, the centrifuge method,[33] and the cloud-point method. In the hypertectic region ($x_{Et_4NBr} > 0.44$), no clear liquidus peaks could be recognized with DSC owing to the low dissolution rates of Et_4NBr, similar to Et_4NI. The solidus enthalpy did not show a clear trend with composition, inhibiting the construction of a Tammann plot. Nonetheless, the three analysis methods allowed for a complementary construction of the phase diagram up to 413 K. The phase transitions were confirmed by the WAXS patterns of the solid fractions that were studied as a function of temperature at three key-compositions (Figs. S21–S23). No solid solution or co-crystal formation was observed; therefore, simple eutectic behavior was assumed for GluA + Et_4NBr as well.

3. Glutaric acid + tetraethylammonium chloride

The phase diagram of GluA + Et_4NCl (Fig. 6) shows that the chloride salt induces the strongest GluA melting point depression. Similar to the GluA + Et_4NBr system, GluA + Et_4NCl mixtures showed limited crystallization owing to supercooling. In fact, none of the prepared samples fully crystallized, neither at low cooling/heating rates (<0.5 K min^{-1}) nor after equilibration at 255 K for 1 week. As a result, no clear solidus peak was observed with DSC for any of the studied GluA + Et_4NCl mixtures (Fig. S24). WAXS patterns (Figs. S28–S31) confirmed the lack of eutectic crystals in the mixtures that did exhibit partial crystallization upon cooling (Fig. S26). After method optimization, a weak endothermic peak was observed at $x_{Et_4NCl} = 0.321$, which might be ascribed to the solidus transition (supplementary material, Sec. 3.3 and Fig. S27).

Above the solidus temperature, other endothermic transitions emerged; at higher compositions ($0.720 < x_{Et_4NCl} < 0.947$), only one transition was observed. The intensity of the DSC peak decreased with increasing salt content, indicating that GluA is involved with the transition. At $T < 295$ K and $x_{Et_4NCl} = 0.74$, the WAXS patterns in Fig. S31 do not clearly correspond to pure GluA or one of the mesophases of Et_4NCl. Hence, a co-crystal with a lower melting point than the liquidus temperature might have formed. The transitions at $x_{Et_4NCl} < 0.7$ are briefly discussed in Sec. 3.3 of the supplementary material. Considering the rather limited impact of the observed transitions on the liquidus phase boundary, the exact mechanisms were not further investigated.

As expected, both the excess GluA and Et_4NCl show S–S transitions corresponding to their pure components for $T > 295$ K. However, no transitions were observed with DSC for compositions $0.45 < x_{Et_4NCl} < 0.6$. The cloud-point and centrifuge methods could not be applied at these compositions, as the temperature control was not reliable below ambient temperature. Hence, GluA + Et_4NCl exhibits such strong melting point depressions that the analysis of the solidus and liquids transition was complicated by supercooling and lower temperature limits of the analyses.

At compositions outside this supercooled window, the liquidus phase boundary was determined with a complementary combination of analysis methods. At the hypotectic side, the liquidus temperatures obtained with the centrifuge method slightly deviate from the trend observed with DSC. At the hypertectic side of the phase diagram, the DSC signals were very weak (Fig. S25). Similar to the other halide salts, slow Et_4NCl dissolution kinetics lead to a restricted heat flow signal. Despite these difficulties, we showed that the combination of analysis techniques—DSC, the cloud-point method, the centrifuge method, and WAXS—offers a toolbox for the construction of eutectic phase diagrams and assignment of the corresponding phase regions.

C. Interpretation of the S-L phase diagrams

While the dilute GluA regime (salt-rich) was inaccessible owing to decomposition, the dilute salt regime could be evaluated and is shown in Fig. 7. Both GluA + Et_4NCl and GluA + Et_4NBr follow ideal eutectic behavior up to relatively high mole fractions, not showing any signs of salt dissociation. For GluA + Et_4NI, quite intriguing behavior was observed: $F_{VtH} = 0.5$ best describes the melting point depression of GluA (Fig. 7). Such low Van 't Hoff factors imply salt aggregation, rather than the ion dissociation observed for Et_4NI in molecular solvents.[44] The quality of the SLE data was evaluated using a framework proposed by NIST;[45] good consistency was observed for GluA + Et_4NCl and GluA + Et_4NBr. The results are summarized in Table S12 and reiterate that $F_{VtH} = 0.5$ is the most consistent with the SLE data of GluA + Et_4NI.

In order to explore the effect of the anion on the complete liquid window, the experimental liquidus phase boundaries were interpolated and extrapolated (Fig. 8, Table I) using the models described in Sec. III. Decomposition hampered the direct measurement of the fusion properties of the three salts involved. The model parameters were therefore obtained by fitting the hypotectic (GluA-rich) side of the phase diagram only. Subsequently, these parameters were used to estimate the salt fusion properties and to construct the corresponding hypertectic liquidus boundaries ($x_{Et_4NX} \to 1$). For clarity, the activity coefficient data in Fig. 8 were limited to the hypotectic side (see Fig. S32 for the full range).

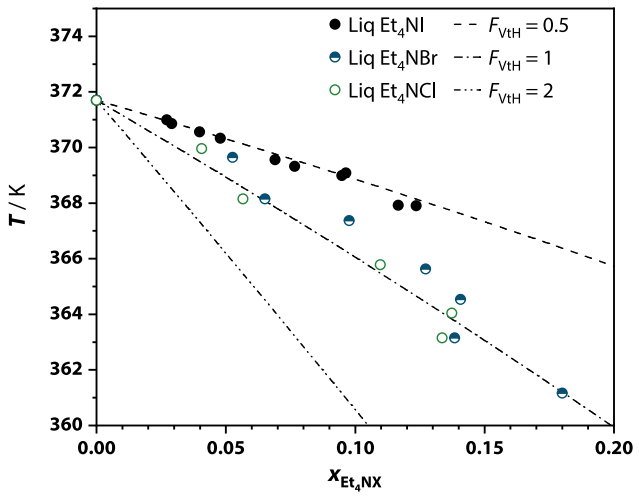

FIG. 7. Liquidus (liq) temperatures (circles) as a function of the salt mole fraction (x_{Et_4NX}) for the glutaric acid + tetraethylammonium halide (GluA + Et_4NX) systems at the diluted salt region. The dashed, dashed-dotted, and dashed-double dotted lines correspond to the ideal liquidus phase boundaries for Van 't Hoff factors (F_{VtH}) of 0.5, 1, and 2, respectively.

Extracting model parameters from the liquidus phase boundary of only one of the components has some implications: (i) The intersection of the two liquidus phase boundaries—the eutectic point—cannot be assessed directly. The solidus data can therefore not be used for the fit, and k_0 (or χ) cannot be determined from the eutectic temperature, contrary to the systems described previously.[31,32] (ii) A relatively narrow region of the phase diagram is used to describe the phase behavior over the full composition range. All data (phase boundaries, activity coefficients, etc.) at compositions beyond that of the fitted region are therefore effectively extrapolations; their physical meaning should be interpreted with care. (iii) Since the invariant eutectic point is absent and a limited amount of data is available, extra care should be taken not to introduce too many degrees of freedom in the g^L models. In this study, the RK polynomial was therefore limited to the first order, and the nonrandomness factor of the NRTL model was fixed at 0.3, both yielding at most two free fitting parameters.

Apparent salt fusion properties were estimated from a linear fit (Fig. S33) of the $\Delta\mu_i/RT$ (or $\log x_i\gamma_i$) vs $1/T$ plot—as described by Lohmann *et al.*[46]—based on the g^L model parameters. All are listed in Table I along with the experimentally obtained decomposition temperatures and S–S transition properties. The extrapolated apparent melting points confirm the experimental observation that these salts melt at temperatures close to or above their decomposition temperature. It should be noted that the most reliable region for this fit—the dilute region of GluA on the salt-rich side—is inaccessible. This is probably the reason that $\Delta_{fus}h_{ap}$ is smaller than the sum of $\Delta_{tr}h$ for the Redlich–Kister-based fits. Hence, if the S–S transitions would be taken into account, a negative enthalpy of fusion would be obtained, which is physically not realistic. Nonetheless, the apparent fusion properties allow for the interpolation of the eutectic point, revealing the most interesting part of the phase diagram: the liquid window below the melting point of GluA.

For all studied mixtures, the first order Redlich–Kister expansion described the hypotectic activity coefficients most accurately (Fig. 8). For GluA + Et_4NCl, the gap between the hypo- and hypertectic liquidus boundaries is significant; hence, considerate differences can be observed between the estimated eutectic points. These differences can be traced back to the unrealistic estimations of salt fusion properties and the narrow composition range at which the liquidus temperatures were accessible. Although the NRTL model does not provide the best description of the corresponding GluA activities, the shape of the hypertectic phase boundary and derived apparent fusion properties seem more realistic than those obtained with the Redlich–Kister polynomials. The apparent fusion temperature is close to the decomposition temperatures, and the apparent enthalpy of fusion is larger than the sum of the S–S transition enthalpies (Table I). This could be explained by the NRTL temperature dependency of g^L, as opposed to Redlich–Kister. The NRTL model is, however, quite sensitive to local minima when minimizing the objective function. The Δg_{12} and Δg_{21} are therefore rarely

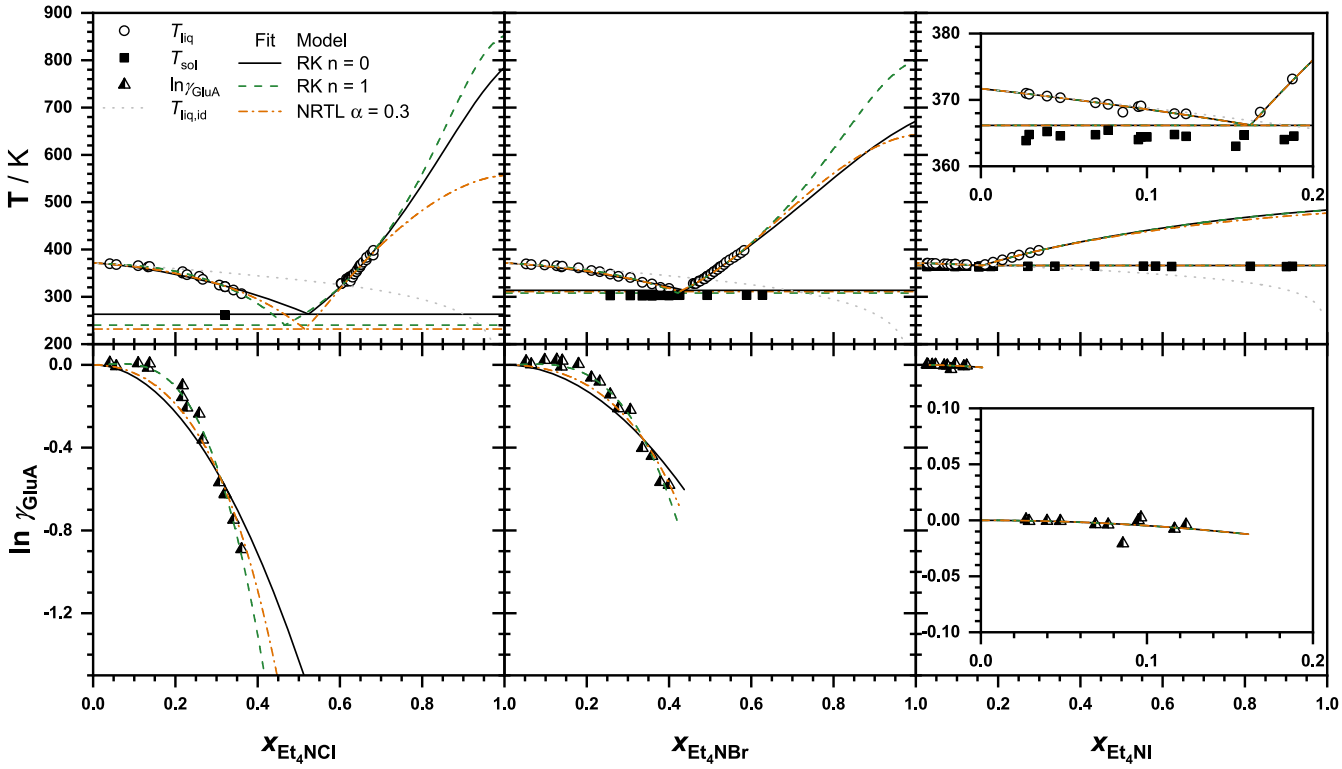

FIG. 8. Model fits to the SLE data (top) and activity coefficients (γ_i, bottom) for the three glutaric acid + tetraethylammonium halide (GluA + Et_4NX) systems studied: GluA + Et_4NCl (left), GluA + Et_4NBr (middle), and GluA + Et_4NI (right, with a Van 't Hoff factor of $i = 0.5$). The symbols represent the liquidus (liq) and solidus (sol) data, as well as ln γ_{GluA} derived from it. The lines are the ideal melting point of GluA (id), the model fits using the Redlich–Kister polynomial (RK) of order n, or the non-random two-liquid (NRTL) model with a non-randomness constant of $\alpha = 0.3$. The insets enlarge the fitted area for GluA + Et_4NI.

a direct measure of the binary interactions, while χ (k_0, Redlich–Kister polynomial) can be interpreted as such.

Interaction parameters χ and k_1 reflect the depth of the eutectic and the difference between the activity coefficient of GluA and the salt at infinite dilute conditions, respectively. When χ is plotted against the ionic radius of the anion, it becomes clear that smaller less polarizable anions lead to stronger intermolecular interactions, leading to stronger negative deviations from ideal eutectic behavior and thus a larger melting point depression (Fig. 9). The effect on χ becomes more pronounced when k_1 is introduced, which

TABLE I. Results of the interpolation and extrapolation of the S–L equilibria for glutaric acid + tetraethylammonium halides (GluA + Et_4NX) using an *n*th-order Redlich–Kister (RK_n) expansion or a non-random two-liquid model with a non-randomness factor of 0.3 ($NRTL_{0.3}$). For each of the Et_4NX salts, the experimental decomposition onset temperatures (T_d) and S–S transition temperatures (T_{tr}) and enthalpies ($\Delta_{tr}h$) are listed. The Van 't Hoff factor was set to 0.5 for GluA + Et_4NI. Fitting parameters p_0 and p_1 correspond to the dimensionless k_0 and k_1 for RK_n, and Δg_{12} and Δg_{21} (J mol^{-1}) for $NRTL_{0.3}$. For each model, the eutectic composition (x_{eut}), eutectic temperature (T_{eut}), sum of residuals (Res), apparent melting points ($T_{fus,ap}$), and apparent fusion enthalpies ($\Delta_{fus}h_{ap}$) are presented.

Salt	T_d (K)	T_{tr} (K)	$\Delta_{tr}h$ (kJ mol^{-1})	Model	p_0	p_1	x_{eut}	T_{eut} (K)	Res (K)	$T_{fus,ap}$ (K)	$\Delta_{fus}h_{ap}$ (kJ mol^{-1})
Et_4NI	493	466.5	23.0	RK_0	−0.9557		0.162	366	5.14	483	31.2
				RK_1	−0.9557	0.004 39	0.162	366	5.15	483	31.3
				$NRTL_{0.3}$	−2 946	0.01	0.163	366	5.36	477	32.7
Et_4NBr	468	463.3	1.5	RK_0	−3.149		0.438	314	75.3	671	8.9
		440.0	19.1	RK_1	−8.907	−3.512	0.421	308	44.5	799	19.4
				$NRTL_{0.3}$	−29 026	0.178 9	0.425	311	60.5	644	50.9
Et_4NCl	450	395.1	7.2	RK_0	−5.699		0.524	263	147	785	6.4
				RK_1	−17.81	−6.896	0.466	240	100	852	21.0
				$NRTL_{0.3}$	−38 703	0.102 2	0.514	232	142	557	53.6

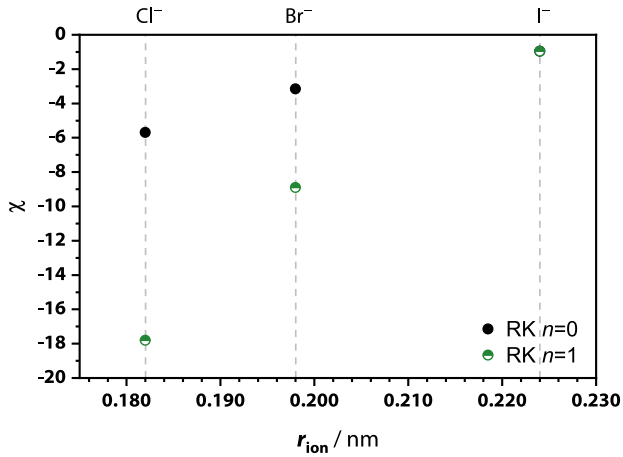

FIG. 9. Binary interaction parameter χ (or k_0) as a function of anionic radius r_{ion}. χ was determined using the Redlich–Kister (RK) polynomial of order n.

essentially represents three-body interactions. This allows for asymmetrical deviations from ideal eutectic behavior through an asymmetric enthalpy of mixing. While χ and k_1 are orthogonal when determined from the full phase diagram,[32] they are not when only the GluA-rich side is used for the fitting due to the implications discussed previously. The large differences between the order of the RK fit are thus a direct result of the unusual ideality of the GluA liquidus phase boundary at $x_{Et_4NX} < 0.2$ (Figs. 7 and 8) and strong non-ideality at $x_{Et_4NX} > 0.2$ (Fig. 8). However, outside the scope of this work, it would be interesting to explore how these observations emerge from the GluA–cation and GluA–anion interactions at different salt contents and how they relate to ion dissociation.

The trend observed for χ in Fig. 9 corroborates the pivotal role of the anion revealed by experimental and molecular simulation studies toward the intermolecular interactions and liquid nanostructures in eutectic mixtures.[7,9–11] The anion is displaced from the ammonium cation via the stabilization of the other constituent. This is controlled by the properties of salt as well as its counterpart, often through complex synergistic routes.[5] For instance, a bulky ammonium cation facilitates the displacement of a chloride anion to a less bulky cation, yielding strong negative deviations from ideal behavior,[9] while for mixtures of similar salts with fatty acids, the alkyl-chain length of the cations showed a minor effect.[6]

Similar to the aforementioned systems, hydrogen bonding between GluA and the halide anion might facilitate a displacement of the latter from the Et_4N^+ cation. Smaller anions are easier to transfer and form stronger hydrogen bonds owing to their higher electronegativity and lower polarizability. This might explain the observed trends in Fig. 9. An in-depth study toward the liquid nanostructure of quaternary ammonium iodide salts in molten acids using molecular dynamics simulations or neutron scattering experiments is outside the scope of this work. We do recognize, however, that studying similar systems on a molecular scale could elucidate the anticipated influence of anion displacement on thermodynamic bulk properties, such as the deviation from ideal eutectic behavior. The transferability of the observed χ–r_{ion} relationship to small non-halide anions, such as nitrate or hydroxide, is yet to be confirmed.

V. CONCLUDING REMARKS

This comprehensive experimental study toward the binary mixtures of glutaric acid (GluA) and tetraethylammonium halide salts (Et_4NX) confirms that the anion plays a pivotal role in the formation of eutectic mixtures containing functionalized ammonium salts. The large polarizable iodide anion shows positive deviations from ideal eutectic behavior, best described with an unusual Van 't Hoff factor of 0.5. Replacing iodide with the smaller less polarizable bromide or chloride anion yields significant negative deviations from ideal eutectic behavior and a large melting point depression. For GluA + Et_4NCl, the eutectic point was shifted below experimentally accessible temperatures. Since all studied ammonium salts decompose before melting, their fusion properties had to be estimated from the GluA-rich side of the phase diagram. As a result, the values for the apparent salt fusion properties and derived hypertectic phase boundaries are uncertain and their physical meaning is limited. Nevertheless, this approach allowed us to evaluate the eutectic point for all systems.

Thermodynamic evaluation of the studied systems revealed that the binary intermolecular interactions become stronger when decreasing the anionic radius. A possible explanation can be found in charge delocalization of the anion. While adding the iodide salt to GluA does not lower the Gibbs energy, bromide and chloride seem to be stabilized via the formation of hydrogen bonds with GluA, lowering the Gibbs energy of the acid as well as the salt. This suggests that the eutectic depth is for a large part controlled by the nature of the anion and its preferential interactions with either the cation or the molecular counterpart. The anion can therefore be considered as an important design parameter that allows the transformation from ideal eutectic mixtures toward deep eutectic systems.

SUPPLEMENTARY MATERIAL

See the supplementary material for an extensive discussion on the thermal analysis using DSC and the centrifuge method. Also included are the ^{1}H-NMR peak assignments, tabulated pure component properties and their corresponding thermograms and WAXS spectra, tabulated phase diagram data and their corresponding thermograms and WAXS spectra, and tabulated fitting parameters and corresponding thermodynamic modeling details.

ACKNOWLEDGMENTS

We are grateful to Sietske de Louw and Mégane Maignan for their experimental efforts in constructing the S–L phase diagrams and Professor G. de With for discussions on the thermodynamic modeling. AvdB would like to thank Dr. ir. P. J. T. Verheijen for his help with the numerical fitting procedures. Financial support from the Netherlands Organization for Scientific Research (NWO) and the company Paques B.V. (Balk, The Netherlands) is gratefully acknowledged. This work is part of the research program "MES meets DES" with Project No. STW–Paques 12999.

DATA AVAILABILITY

The data that support the findings of this study are available within the article and its supplementary material. Raw signals (DSC thermograms, WAXS patterns, NMR spectra, and TGA) are available from the corresponding author upon reasonable request.

REFERENCES

[1] A. P. Abbott, G. Capper, D. L. Davies, R. K. Rasheed, and V. Tambyrajah, Chem. Commun. **2003**, 70.
[2] J. Jacquemin, M. Bendová, and E. Waghorne, J. Solution Chem. **89**, 579 (2019).
[3] B. B. Hansen, S. Spittle, B. Chen, D. Poe, Y. Zhang, J. M. Klein, A. Horton, L. Adhikari, T. Zelovich, B. W. Doherty, B. Gurkan, E. J. Maginn, A. Ragauskas, M. Dadmun, T. A. Zawodzinski, G. A. Baker, M. E. Tuckerman, R. F. Savinell, and J. R. Sangoro, Chem. Rev. **121**, 1232 (2021).
[4] M. A. R. Martins, S. P. Pinho, and J. A. P. Coutinho, J. Solution Chem. **48**, 962 (2019).
[5] L. J. B. M. Kollau, R. Tuinier, J. Verhaak, J. den Doelder, I. A. W. Filot, and M. Vis, J. Phys. Chem. B **124**, 5209 (2020).
[6] P. V. A. Pontes, E. A. Crespo, M. A. R. Martins, L. P. Silva, C. M. S. S. Neves, G. J. Maximo, M. D. Hubinger, E. A. C. Batista, S. P. Pinho, J. A. P. Coutinho, G. Sadowski, and C. Held, Fluid Phase Equilib. **448**, 69 (2017).
[7] O. S. Hammond, D. T. Bowron, and K. J. Edler, Green Chem. **18**, 2736 (2016).
[8] F. Crea, A. De Robertis, and S. Sammartano, J. Solution Chem. **33**, 499 (2004).
[9] D. O. Abranches, N. Schaeffer, L. P. Silva, M. A. R. Martins, S. P. Pinho, and J. A. P. Coutinho, Molecules **24**, 3687 (2019).
[10] M. Gilmore, L. M. Moura, A. H. Turner, M. Swadźba-Kwaśny, S. K. Callear, J. A. McCune, O. A. Scherman, and J. D. Holbrey, J. Chem. Phys. **148**, 193823 (2018).
[11] M. E. Di Pietro, O. Hammond, A. van den Bruinhorst, A. Mannu, A. Padua, A. Mele, and M. Costa Gomes, Phys. Chem. Chem. Phys. **23**, 107 (2021).
[12] G. Berchiesi, A. Cingolani, and D. Leonesi, J. Therm. Anal. **6**, 91 (1974).
[13] G. G. Lobbia, G. Berchiesi, and M. A. Berchiesi, J. Therm. Anal. **10**, 137 (1976).
[14] E. A. Drylie, D. S. Wragg, E. R. Parnham, P. S. Wheatley, A. M. Z. Slawin, J. E. Warren, and R. E. Morris, Angew. Chem., Int. Ed. **46**, 7839 (2007).
[15] K. D. Beyer, C. S. Pearson, and D. S. Henningfield, J. Phys. Chem. A **117**, 3630 (2013).
[16] C. Florindo, F. S. Oliveira, L. P. N. Rebelo, A. M. Fernandes, and I. M. Marrucho, ACS Sustainable Chem. Eng. **2**, 2416 (2014).
[17] A. V. Kolyado, S. M. Alenova, and I. K. Garkushin, Russ. J. Phys. Chem. A **90**, 1293 (2016).
[18] D. P. McNamara, S. L. Childs, J. Giordano, A. Iarriccio, J. Cassidy, M. S. Shet, R. Mannion, E. O'Donnell, and A. Park, Pharm. Res. **23**, 1888 (2006).
[19] N. Qiao, M. Li, W. Schlindwein, N. Malek, A. Davies, and G. Trappitt, Int. J. Pharm. **419**, 1 (2011).
[20] B. A. Zakharov, E. A. Losev, B. A. Kolesov, V. A. Drebushchak, and E. V. Boldyreva, Acta Crystallogr., Sect. B: Struct. Sci. **68**, 287 (2012).
[21] L. Bian, H. Zhao, H. Hao, Q. Yin, S. Wu, J. Gong, and W. Dong, Chem. Eng. Technol. **36**, 1292 (2013).
[22] B. C. Félix-Sonda, J. Rivera-Islas, D. Herrera-Ruiz, H. Morales-Rojas, and H. Höpfl, Cryst. Growth Des. **14**, 1086 (2014).
[23] K. Chadwick, R. Davey, G. Sadiq, W. Cross, and R. Pritchard, CrystEngComm **11**, 412 (2009).
[24] N. Rodriguez Rodriguez, A. van den Bruinhorst, L. J. B. M. Kollau, M. C. Kroon, and K. Binnemans, ACS Sustainable Chem. Eng. **7**, 11521 (2019).
[25] A. van den Bruinhorst, in *Deep Eutectic Solvents: A New Generation of Designer Solvents* (Technische Universiteit Eindhoven, 2018), Chap. 4, pp. 84–171.
[26] W. V. Steele, R. D. Chirico, A. B. Cowell, S. E. Knipmeyer, and A. Nguyen, J. Chem. Eng. Data **47**, 725 (2002).
[27] P. Espeau, P. Négrier, and Y. Corvis, Cryst. Growth Des. **13**, 723 (2013).
[28] B. Szafrańska and Z. Pajak, J. Mol. Struct. **99**, 147 (1983).
[29] A. Xenopoulos, J. Cheng, M. Yasuniwa, and B. Wunderlich, Mol. Cryst. Liq. Cryst. Sci. Technol., Sect. A **214**, 63 (1992).
[30] H. M. Powell and E. Wait, J. Chem. Soc. **1958**, 1866.
[31] L. J. B. M. Kollau, M. Vis, A. van den Bruinhorst, A. C. C. Esteves, and R. Tuinier, Chem. Commun. **54**, 13351 (2018).
[32] L. J. B. M. Kollau, M. Vis, A. van den Bruinhorst, G. de With, and R. Tuinier, Pure Appl. Chem. **91**, 1341 (2019).
[33] A. van den Bruinhorst, L. J. B. M. Kollau, M. C. Kroon, J. Meuldijk, R. Tuinier, and A. C. C. Esteves, J. Chem. Phys. **149**, 224505 (2018).
[34] P. W. Atkins and J. de Paula, *Atkins' Physical Chemistry* (Oxford University Press, Oxford, UK, 2006).
[35] O. Redlich and A. T. Kister, J. Chem. Phys. **15**, 849 (1947).
[36] H. Renon and J. M. Prausnitz, AIChE J. **14**, 135 (1968).
[37] M. Margules, Sitzungsber. Kais. Akad. Wiss. Wien Math. Kl. II **104**, 1243 (1895).
[38] J.-M. Ha, B. D. Hamilton, M. A. Hillmyer, and M. D. Ward, Cryst. Growth Des. **9**, 4766 (2009).
[39] D. J. Good and N. Rodríguez-Hornedo, Cryst. Growth Des. **9**, 2252 (2009).
[40] M. Sawicka, P. Storoniak, J. Błażejowski, and J. Rak, J. Phys. Chem. A **110**, 5066 (2006).
[41] R. A. Mackay, J. Levkov, and W. Kohr, J. Phys. Chem. **75**, 2066 (1971).
[42] J. Cheng, A. Xenopoulos, and B. Wunderlich, Mol. Cryst. Liq. Cryst. Sci. Technol. Sect. A. Mol. Cryst. Liq. Cryst. **220**, 127 (1992).
[43] F. A. e Silva, J. F. B. Pereira, K. A. Kurnia, S. P. M. Ventura, A. M. S. Silva, R. D. Rogers, J. A. P. Coutinho, and M. G. Freire, Chem. Commun. **53**, 7298 (2017).
[44] A. R. Martin, J. Chem. Soc. **1930**, 530.
[45] J. W. Kang, V. Diky, R. D. Chirico, J. W. Magee, C. D. Muzny, A. F. Kazakov, K. Kroenlein, and M. Frenkel, J. Chem. Eng. Data **59**, 2283 (2014).
[46] J. Lohmann, R. Joh, and J. Gmehling, J. Chem. Eng. Data **42**, 1176 (1997).